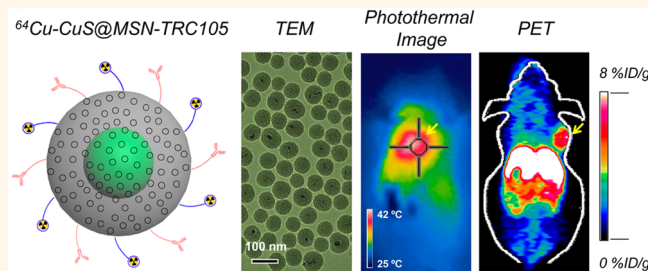


In Vivo Tumor Vasculature Targeting of CuS@MSN Based Theranostic Nanomedicine

Feng Chen,^{†,‡} Hao Hong,^{†,‡} Shreya Goel,[‡] Stephen A. Graves,[§] Hakan Orbay,[†] Emily B. Ehlerding,[§] Sixiang Shi,[‡] Charles P. Theuer,[‡] Robert J. Nickles,[§] and Weibo Cai^{*†,‡,§,||}

[†]Department of Radiology, University of Wisconsin — Madison, Wisconsin 53705, United States, [‡]Materials Science Program, University of Wisconsin — Madison, Wisconsin 53705, United States, [§]Department of Medical Physics, University of Wisconsin — Madison, Wisconsin 53705, United States, ^{||}TRACON Pharmaceuticals, Inc., San Diego, California 92122, United States, and ^{||}University of Wisconsin Carbone Cancer Center, Madison, Wisconsin 53705, United States. ^{*}Feng Chen and Hao Hong contributed equally to this work.

ABSTRACT Actively targeted theranostic nanomedicine may be the key for future personalized cancer management. Although numerous types of theranostic nanoparticles have been developed in the past decade for cancer treatment, challenges still exist in the engineering of biocompatible theranostic nanoparticles with highly specific *in vivo* tumor targeting capabilities. Here, we report the design, synthesis, surface engineering, and *in vivo* active vasculature targeting of a new category of theranostic nanoparticle for future cancer management. Water-soluble photothermally sensitive copper sulfide nanoparticles were encapsulated in biocompatible mesoporous silica shells, followed by multistep surface engineering to form the final theranostic nanoparticles. Systematic *in vitro* targeting, an *in vivo* long-term toxicity study, photothermal ablation evaluation, *in vivo* vasculature targeted imaging, biodistribution and histology studies were performed to fully explore the potential of as-developed new theranostic nanoparticles.



KEYWORDS: vasculature targeting · CuS · mesoporous silica nanoparticle · theranostic nanomedicine · photothermal ablation

A theranostic nanoparticle is a multi-functional nanosystem that is well-designed for specific and personalized disease management by combining diagnostic and therapeutic capabilities into one single biocompatible and biodegradable nanoparticle.¹ Many preclinical studies and clinical trials with peptide- or antibody-conjugated imaging nanoparticles and chemotherapeutics have already demonstrated the value of such specifically targeted imaging and therapy of tumors.^{2–4} Many types of theranostic nanoparticles have been developed in the past decade for treating cancers, based on both organic and inorganic platforms.^{5,6} However, most of these studies have been focused on using passive targeting strategies of tumors based on the enhanced permeability and retention (EPR) effect.^{7,8} To date, engineering of biocompatible theranostic nanoparticles with highly specific *in vivo* tumor active targeting capabilities is still in its very early stages with

only few examples of *in vivo* tumor actively targeted theranostic nanoparticles being reported.⁹

Here, we report surface engineering and *in vivo* vasculature targeting of a new category of theranostic nanoparticle for future cancer management. As shown in Figure 1a, water-soluble copper sulfide (CuS) nanoparticles were selected as the core owing to their strong near-infrared (NIR) optical absorption and high molar extinction coefficient ($8.66 \times 10^7 \text{ cm}^{-1} \text{ M}^{-1}$ at 930 nm, ~11 nm sized).¹⁰ Shell-thickness and pore-size controllable mesoporous silica nanoshells (MSN) were introduced as not only a protective shell, but also an anticancer drug reservoir for potential targeted drug delivery and thermal-chemotherapy (Step 1 in Figure 1a). As-synthesized CuS@MSN was then surface engineered with amino groups ($-\text{NH}_2$), NOTA (1,4,7-triazacyclononane-triacetic acid, a well-known chelator for copper-64 [⁶⁴Cu] labeling), polyethylene

* Address correspondence to
wcai@uwhs.org.

Received for review December 18, 2014
and accepted April 5, 2015.

Published online April 06, 2015
10.1021/nn507241v

© 2015 American Chemical Society

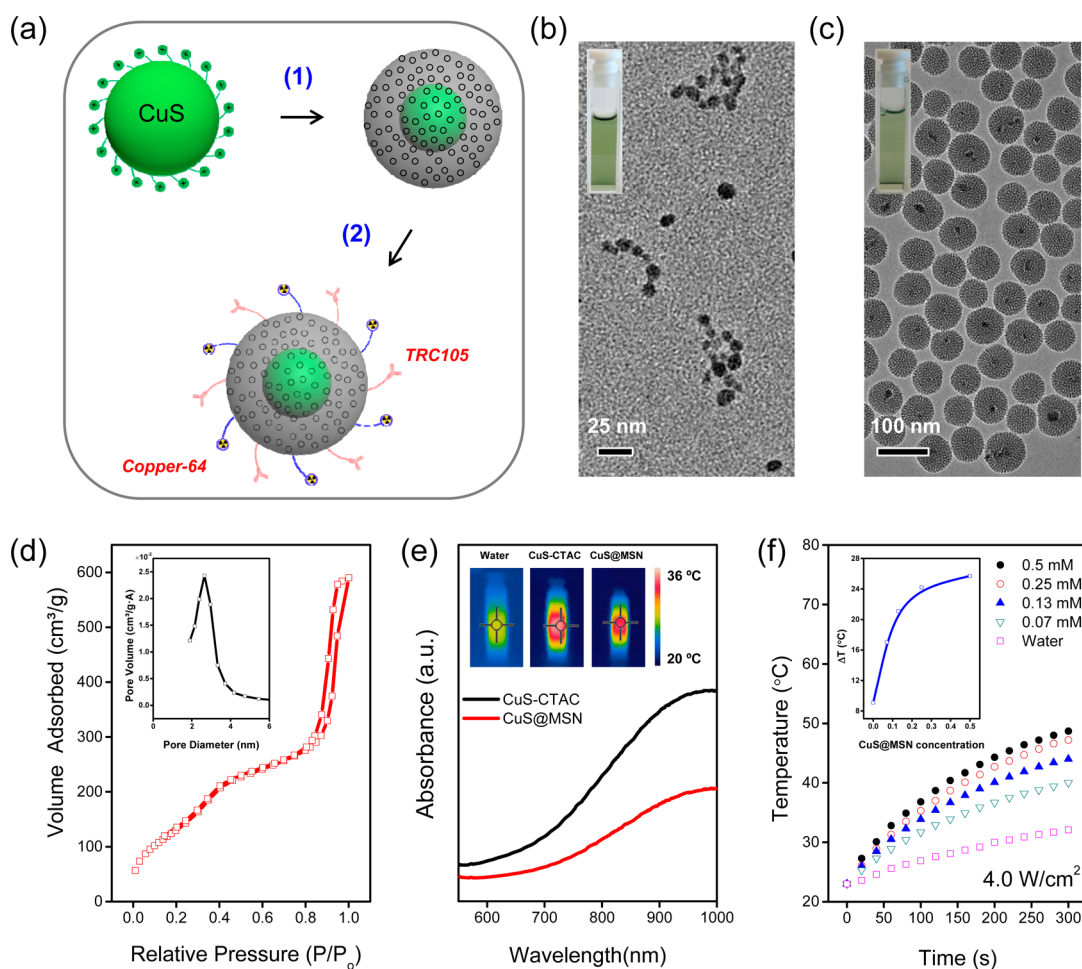


Figure 1. Synthesis and characterization of CuS@MSN. (a) A schematic illustration showing 3 major steps for the synthesis of ^{64}Cu -CuS@MSN-TRC105 theranostic nanoparticle. Step 1: encapsulating CuS-CTAC inside mesoporous silica shell, resulting in CuS@MSN nanoparticle. Step 2: surface engineering of CuS@MSN to form ^{64}Cu -CuS@MSN-TRC105 nanoconjugates (see Figure S1 for more details). (b) A TEM image of CuS-CTAC. Inset shows the digital photo of CuS-CTAC in water. (c) A TEM image of CuS@MSN. Inset shows the digital photo of CuS@MSN in water. (d) Nitrogen adsorption–desorption isotherms and the corresponding pore size distribution of CuS@MSN (inset, see Figure S4 for enlarged figure). (e) UV–vis absorption spectra of CuS-CTAC (black line) and CuS@MSN (red line). Inset shows the photothermal images of water, CuS-CTAC and CuS@MSN (from left to right) (see Figure S5 for enlarged figure). Note, both CuS-CTAC and CuS@MSN have the same amount of CuS nanoparticles (*i.e.*, 0.25 mM of Cu based on ICP-AES measurement). (f) Quantitative temperature change of CuS@MSN aqueous solution as a function of 980 nm laser exposure time (laser power density: 4.0 W/cm²). Concentration of CuS@MSN was based on total Cu amount measured by using ICP-AES. Inset shows the increased temperature for samples with varied CuS@MSN concentrations (see Figure S6 for enlarged figure).

glycol (PEG, for improved *in vivo* biocompatibility and stability), TRC105 (a human/murine chimeric IgG1 monoclonal antibody, which binds to both human and murine CD105 on tumor neovasculature),¹¹ and finally the radioisotope ^{64}Cu (a positron emitter with a 12.7 h half-life, for positron emission tomography [PET] imaging and biodistribution studies) (Step 2 in Figure 1a, also see Figure S1, Supporting Information, for more details). Note, since all the CuS@MSN conjugates contain the same NOTA and PEG chains (5 kDa), both “NOTA” and “PEG” were omitted from the acronyms of the final conjugates for clarity considerations.

RESULTS AND DISCUSSION

Synthesis and Characterization of CuS@MSN. Sodium citrate-capped CuS (*i.e.*, CuS-Cit) nanoparticles, or CuS

with other varied morphologies, are part of a relatively new class of photothermal agents with attractive photothermal ablation properties, due to their behavior as p-type semiconductors.^{10,12,13} Silica (or silicon dioxide) is “generally recognized as safe” by the Food and Drug Administration (FDA, ID Code: 14808–60–7),¹⁴ which is highly desirable for future clinical translation. Mesoporous silica nanoparticles exhibit controllable pore size, high specific surface area, large pore volume, and well-established surface modification chemistry,¹⁵ and have thus been accepted as highly attractive drug carriers since 2001.¹⁶

Our initial attempt to encapsulate CuS-Cit nanoparticles into MSN was not successful (Figure S2b), possibly due to its negatively charged surface (zeta potential: -21.3 ± 4.0 mV, Figure S3a). To facilitate the

coating of MSN over CuS, positively charged cetyltrimethylammonium chloride (*i.e.*, CTAC) stabilized CuS (*i.e.*, CuS-CTAC) was used instead. Figure 1b shows the representative transmission electron microscopy (TEM) image of CuS-CTAC with an average particle size of \sim 10 nm. Dynamic light scattering (DLS) and zeta potential measurements showed a slightly increased particle size of 18.3 ± 0.2 nm, and 33.4 ± 1.3 mV of surface charge.

It is worthwhile to note that the surfactant CTAC functions as not only the capping agent for stabilizing the CuS nanoparticles, but also as the template for the successful growth of the mesoporous silica shell over CuS. Figure 1c shows the TEM image of core@shell structured CuS@MSN with an average particle size of 65 nm (detailed synthetic procedures can be found in the Supporting Information). The amount of extra CTAC used plays a significant role in controlling the size, yield, and monodispersity of CuS@MSN. Our results showed that higher yield and smaller-sized CuS@MSN (30–40 nm) could be achieved by reducing the CTAC (25 wt % solution) amount from 2 g (or \sim 20 mg/mL by concentration) to 0.5 g (or \sim 5 mg/mL by concentration) (Figure S7c), while only CuS@MSN with severe aggregations could be obtained if no extra CTAC was used (Figure S7d). The template CTAC was then removed by stirring the nanoparticles in 1 wt % solution of NaCl in methanol at room temperature for 3 days. Fourier transform infrared spectroscopy was later performed to confirm the successful and complete removal of CTAC, as evidenced by the absence of characteristic C–H peak in the 3000–2800 cm^{-1} wavelength range for surfactant-extracted CuS@MSN (Figure S8).¹⁷ Nitrogen adsorption–desorption isotherm results further indicate that as-synthesized CuS@MSN possesses significantly higher specific surface areas ($495 \text{ m}^2/\text{g}$) and larger pore volume ($0.68 \text{ cm}^3/\text{g}$) than that of previously reported similar structure (surface areas: $221 \text{ m}^2/\text{g}$, pore volume: $0.22 \text{ cm}^3/\text{g}$) (Figure 1d).¹⁸ Average pore sizes was further found to be \sim 2.2 nm (Figure 1d), holding great potential for anticancer drug delivery.

Anticancer Drug Loading, Releasing and Photothermal Ablation Properties of CuS@MSN. Next, we demonstrated that with the coating of MSN, as-synthesized CuS@MSN not only preserved the photothermal ablation property, but could also be used as an anticancer drug delivery system. The small molecule anticancer drug doxorubicin (DOX) was selected as the model drug, and was loaded into CuS@MSN by mixing them together in phosphate buffered saline (PBS) solution under shaking. The loading capacity of DOX was found to be as high as 465.1 mg/g after 24 h incubation. Due to the decrease in the electrostatic interaction between DOX and silica with the decrease of pH value,¹⁹ CuS@MSN(DOX) also showed a fast release rate at pH 5 when compare with that at pH 7.4 (as shown in

Figure S9). This holds great potential for future pH-sensitive drug delivery, considering that tumor cell (lysosomes: pH 4–5, endosomes: pH 5–6) or tumor microenvironment (pH 6.5–7.2) has a lower pH value (caused by hypoxia) when compared with that in bloodstream (pH 7.4).²⁰

Although an 808 nm laser was first used for triggering the photothermal ablation of CuS nanoparticles,¹⁰ a recent study demonstrated that a 980 nm laser may become a better choice due to the higher absorbance of CuS at 980 nm, deeper tissue penetration depth, and higher conservative limit for human skin (\sim 0.726 vs \sim 0.33 W/cm²).¹³ The successful synthesis of CuS-CTAC and CuS@MSN was further confirmed by their characteristic green color (insets in Figure 1b,c) and strong absorption peak at around 980 nm from the UV–vis absorbance spectra (Figure 1e). As shown in Figure S10b, nearly 100% of 980 nm light was absorbed by CuS@MSN (0.5 mM, based on total amount of Cu measured by using inductively coupled plasma atomic emission spectroscopy [ICP-AES]), as evidenced by the disappearance of the laser spot from the near-infrared (IR) card. Efficient energy conversion from light to heat was also confirmed by their photothermal images (Figure 1e, inset) with the control water sample showing only slightly increased temperature after the same laser irradiation.

The quantitative temperature change of the CuS@MSN aqueous solution as a function of laser exposure time was also investigated. As shown in Figure 1f, a total increase of 25 °C was observed after exposing CuS@MSN (0.5 mM) to the 980 nm laser light (a continuous wave fiber-coupled laser, 4 W/cm²) for 5 min, while an increase of only 9 °C was observed in the pure water control group (due to the thermal effect of 980 nm laser²¹). As expected, the 980 nm light-induced thermal effect is highly dependent on both the concentration of CuS@MSN in water and the laser dose (power density and exposure time). Water-soluble CuS@MSN with the highest concentration (*e.g.*, 0.5 mM) under the exposure to 980 nm laser with a high power density (*e.g.*, 4 W/cm²) showed the most significant thermal effect when compared with samples with lower concentration under excitation of the 980 nm laser with reduced power density (Figure S11).

The *in vivo* photothermal ablation of tumors was also demonstrated after a single intratumoral injection of CuS@MSN in 4T1 tumor-bearing mice ($n = 5$, dose: 33 mg/kg). Tumors were irradiated with the 980 nm laser (4 W/cm²) for 15 min, followed by size measurement with a caliper every other day. Two control groups, CuS@MSN only and 980 nm laser only, were also introduced to better demonstrate the photothermal ablation property. As shown in the photothermal images in Figures 2a–c, significant temperature increase from 25 to >42 °C was observed in the CuS@MSN+980 nm laser group, while the 980 nm laser

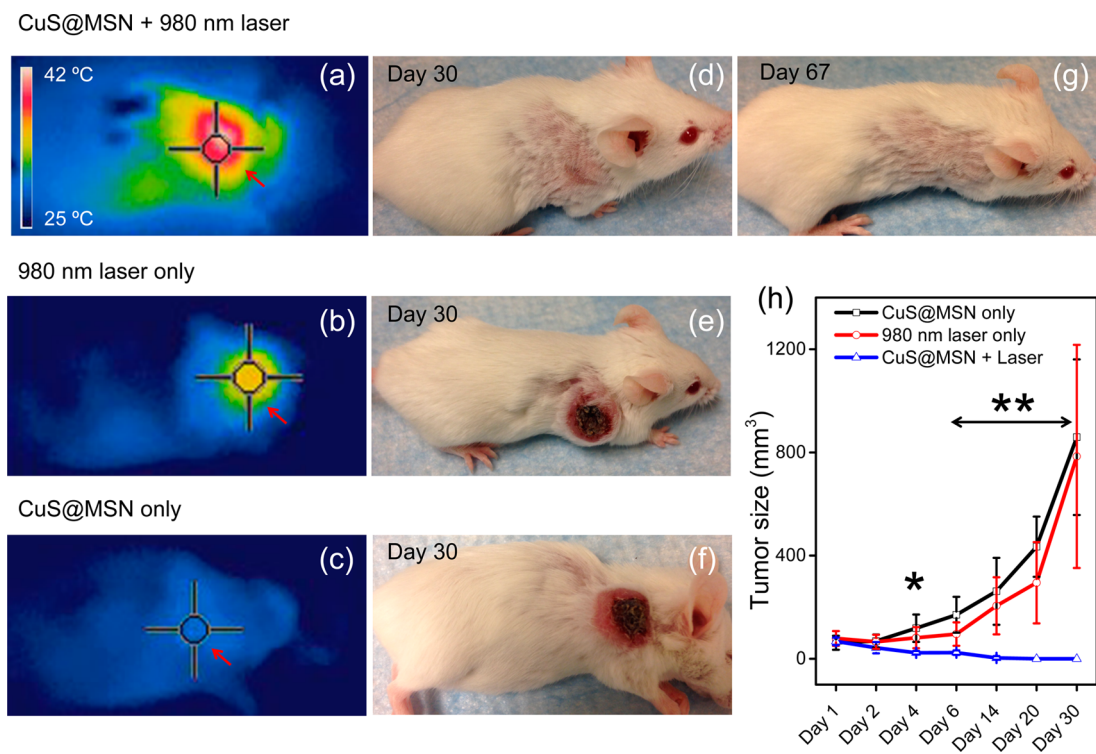


Figure 2. *In vivo* photothermal therapeutic evaluation. Photothermal images of mice after laser treatment. (a) (**CuS@MSN+980 nm laser**) group, (b) (**980 nm laser only**) group, and (c) (**CuS@MSN only**) group. Digital photos of mice with 4T1 tumors on Day 30 after treatment. (d) (**CuS@MSN+980 nm laser**) group, (e) (**980 nm laser only**) group, and (f) (**CuS@MSN only**) group. (g) A digital photo of mouse from (**CuS@MSN+980 nm laser**) group on Day 67 after treatment. (h) Changes of tumor size of mice from 3 different groups after treatment ($n = 5$). Laser dose: 4 W/cm^2 , 15 min. CuS@MSN dose: 33 mg/kg . Tumors were marked with red arrows. The differences between the treatment group and two control groups were statistically significant (* $P < 0.05$ on Day 4, ** $P < 0.01$ at later time points).

only group showed only slightly increased skin temperature due to the 980 nm laser thermal effect, clearly indicating the photothermal effect of CuS@MSN *in vivo*. After laser treatment, dark-red skin at the tumor site was observed in both the CuS@MSN+980 nm laser and 980 nm laser only groups, suggesting tissue burns caused by the local photothermal effect. Decreases in the tumor size in these two groups were also observed with a more prominent shrinking rate found in the CuS@MSN+980 nm laser group during the first 4 days (Figure S12). Tumors from CuS@MSN+980 nm laser group continued to shrink, and completely vanished on Day 14 with no regrowth in the next 67 days (Figure 2d,g). In comparison, tumors started regrowing after Day 4 in the 980 nm laser only group (Figure 2h, S12), and continued to grow rapidly over the next 30 days. No initial tumor shrinkage and only rapid growth were observed in the CuS@MSN only group. Taken together, these studies demonstrated the potential of using CuS@MSN as an anticancer drug carrier as well as an *in vivo* photothermal ablation agent.

In Vitro CD105 Targeting and *In Vivo* Long-Term Toxicity Studies. CD105 (also known as endoglin) is considered one of the most reliable markers for the proliferation of endothelial cells, and is overexpressed on most tumor neovasculature.^{22,23} TRC105 is a CD105-targeted antibody with a very high avidity for human CD105

(K_D : 2 ng/mL). TRC105 has been used for PET imaging of CD105 in a variety of disease models, including cancers, hindlimb ischemia, and myocardial infarction models.^{24–26} The successful targeting of functional nanoparticles such as graphene oxide,²⁷ porous silica nanoparticles,^{28,29} and micelles³⁰ has also been demonstrated recently, making TRC105-based vasculature targeting a highly attractive strategy for cancer theranostics. Here, the TRC105 antibody was selected for *in vitro* and *in vivo* CD105 targeting of CuS@MSN nanocomposites.

Before the *in vivo* tumor targeted imaging, human umbilical vein endothelial cells (HUVECs, CD105 positive) were used in a flow cytometry study to confirm the *in vitro* CD105 targeting efficiency of the TRC105 conjugated CuS@MSN. CuS@MSN modified with amino groups was first conjugated with NHS-fluorescein, and then with TRC105 to facilitate the flow cytometry investigation. Our results from Figure 3a indicate that incubation with the fluorescein conjugated CuS@MSN-TRC105 (targeted group) significantly enhanced the mean fluorescence intensity of HUVECs. On the other hand, treating with fluorescein conjugated CuS@MSN (nontargeted group), or fluorescein conjugated CuS@MSN-TRC105 with a blocking dose of TRC105 ($500 \mu\text{g/mL}$, blocking group), only gave minimal fluorescence enhancement. Successful CD105

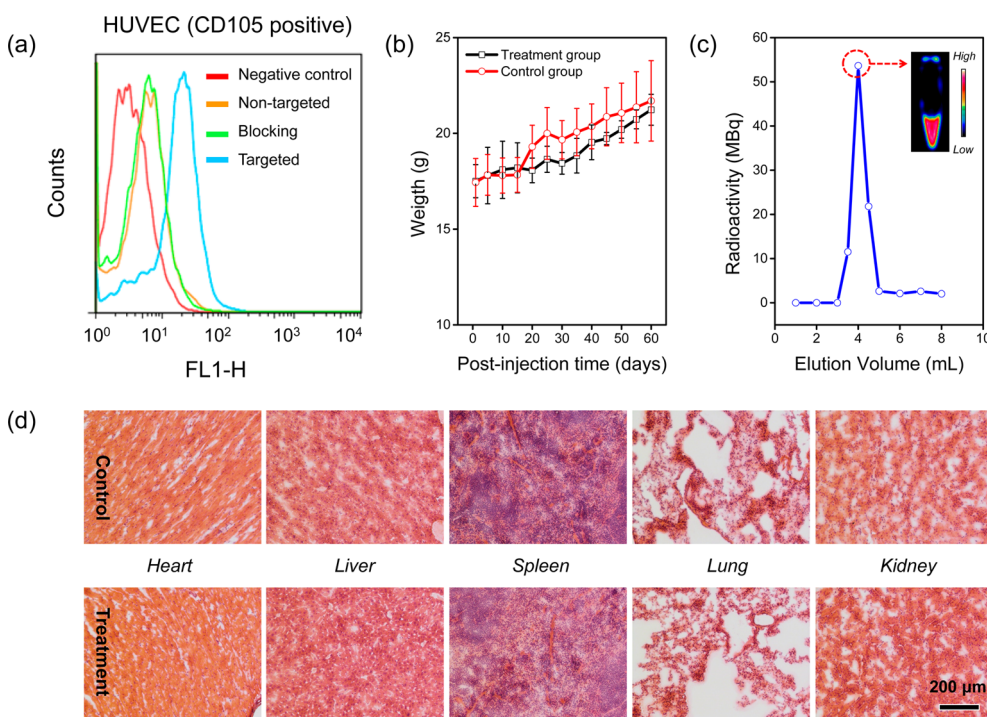


Figure 3. *In vitro* CD105 targeting, long-term toxicity and radiolabeling studies. (a) Flow cytometry analysis of CuS@MSN nanoconjugates in HUVEC (CD105 positive) cell lines (incubation time was set at 30 min). (b) Two-month growth chart of mice from treatment (dose: 90 mg/kg of PEGylated CuS@MSN in PBS) and control groups (PBS only). (c) A size-exclusion column chromatography elution profile during the purification of ⁶⁴Cu-CuS@MSN-TRC105. The unreacted ⁶⁴Cu elutes after 6 mL. Inset shows the PET imaging of fraction 3.5–4.0 mL. (d) H&E-stained tissue sections from mice injected with PEGylated CuS@MSN (treatment group) and PBS only (control group) after 60 days. Tissues were harvested from heart, liver, spleen, lung and kidney.

targeting of CuS@MSN-TRC105 was demonstrated *in vitro* through these studies.

An *in vivo* long-term toxicity study was then performed in healthy female BALB/c mice (weight: ~18 g, n = 3) by monitoring fluctuations in body weight. Each mouse was intravenously injected with PEGylated CuS@MSN (dispersed in 200 μL of PBS) at a high dose of 90 mg/kg, followed by weight monitoring every other day for over two months. Mice injected with only PBS were served as the control group. As shown in Figure 3b, similar body weight increases were observed for both groups during the first 2 weeks, suggesting that all mice continued to mature without noticeable toxicity effects. After 2 weeks, a small weight difference (4–7%) between the two groups was observed, indicating the low toxicity of high dose PEGylated CuS@MSN *in vivo*. On Day 60, the body weight difference decreased to <2%, suggesting most of the PEGylated CuS@MSN might have been excreted. No changes in food intake, water consumption, fur color, exploratory behavior, activity, and neurological status were observed.

A histological assessment of tissues from the heart, liver, spleen, lung, and kidney was conducted after Day 60 to further investigate potential signs of toxicity (*i.e.*, cellular shrinkage or blebbing, steatosis in liver cells, condensation of chromatin, rupture of cell membrane and apoptotic bodies). Overall, no significant

difference was observed between the treatment and control groups (Figure 3c). Although slight airway wall thickening and increased cellularity in some of the lung slides were observed in the treatment group, there were no signs of the cellular toxicity indicators described above. Such increased cellularity and thickening might be because of nanoparticle accumulation in the interstitial space, which eventually attracted inflammatory cells to the site.³¹ Thus, we demonstrated the *in vitro* CD105 targeting capability of TRC105-conjugated CuS@MSN and the low long-term toxicity of PEGylated CuS@MSN at a high dose. Encouraged by these results, we moved on to investigate the *in vivo* tumor vasculature targeting and biodistribution pattern of ⁶⁴Cu-CuS@MSN-TRC105 nanoconjugates.

In Vivo Vasculature Targeted PET Imaging and Biodistribution Studies. Labeling nanoparticles with positron-emitting radionuclides has been generally recognized as one of the most accurate means for noninvasive evaluation of their biodistribution and pharmacokinetics.³² For *in vivo* tumor vasculature targeted PET imaging, NOTA-conjugated CuS@MSN-TRC105 was labeled with ⁶⁴Cu at 37 °C and purified using PD-10 columns. A typical elution profile is provided in Figure 3c with the inset showing the PET imaging of fraction 3.5–4.0 mL, clearly demonstrating the successful synthesis of ⁶⁴Cu-CuS@MSN-TRC105.

In vivo tumor vasculature targeted PET imaging was then carried out in 4T1 murine breast tumor-bearing

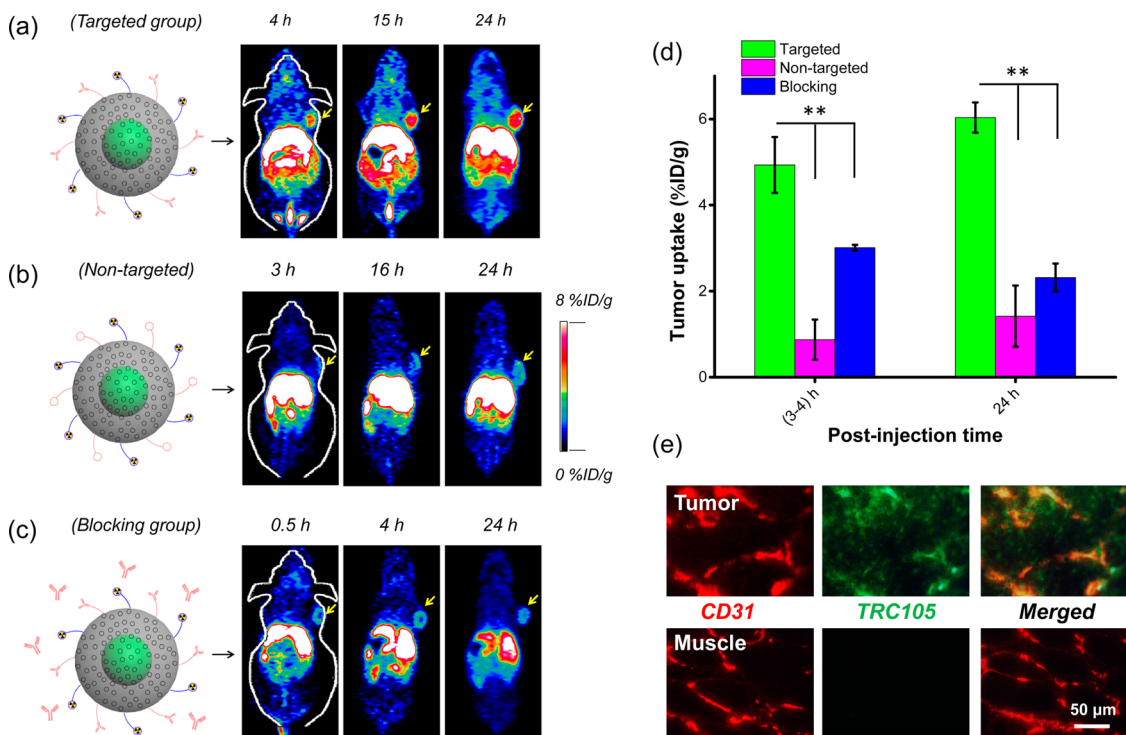


Figure 4. *In vivo* CD105 targeted PET imaging, tumor uptake comparison and histology studies. *In vivo* serial coronal PET images of ^{64}Cu -CuS@MSN-TRC105 nanoconjugates (a, targeted group), ^{64}Cu -CuS@MSN (b, nontargeted group) and ^{64}Cu -CuS@MSN-TRC105 with a large dose of free TRC105 (c, blocking group) in 4T1 murine breast tumor-bearing mice at different time points postinjection. (d) Tumor uptake comparison among 3 different groups. The difference between 4T1 tumor uptake in targeted group and two control groups were statistically significant (** $P < 0.01$). (e) *Ex vivo* histology analysis of the tumor tissue slices with CD31 (red, with antimouse CD31 primary antibody) and CD105 (green, using the TRC105 from ^{64}Cu -CuS@MSN-TRC105 as the primary antibody). Muscle slices were also provided. Tumors were marked with yellow arrows.

mice, which express high level of CD105 on the tumor neovasculature.³³ Each mouse was intravenously injected with 5–10 MBq of ^{64}Cu -CuS@MSN-TRC105 ($\sim 1 \text{ mg/kg}$), and serial PET scans were obtained at 4, 15, and 24 h postinjection (p.i.) to show the tumor targeting efficacy and *in vivo* biodistribution patterns (Figure 4a). The accumulation of ^{64}Cu -CuS@MSN-TRC105 in the 4T1 tumor was found to be $4.9 \pm 0.7\% \text{ ID/g}$ at 4 h p.i., and peaked at $6.0 \pm 0.4\% \text{ ID/g}$ at 24 h p.i., as shown in Figure 4a ($n = 3$). In contrast, without the conjugation of TRC105 (*i.e.*, EPR effect alone), the 4T1 tumor uptake of ^{64}Cu -CuS@MSN was found to be around $1\% \text{ ID/g}$ at all of the time points examined ($n = 3$; Figure 4b), indicating that TRC105 conjugation is likely the controlling factor for enhanced tumor accumulation of ^{64}Cu -CuS@MSN-TRC105. Similar to what we have observed in other TRC105-conjugated nanoparticles,^{27,30} most of ^{64}Cu -CuS@MSN-TRC105 nanoconjugates were taken up by the reticuloendothelial system (RES) with liver uptake found to be $31.3 \pm 1.5\% \text{ ID/g}$ at 4 h p.i., and decreased gradually to $17.1 \pm 0.9\% \text{ ID/g}$ at 24 h p.i. ($n = 3$). An *ex vivo* biodistribution study at 24 h p.i. further confirmed such dominant liver uptake, as shown in Figure S13.

To study the CD105 targeting specificity of ^{64}Cu -CuS@MSN-TRC105 *in vivo*, blocking studies were performed. Results showed that administration of a

blocking dose (1 mg/mouse) of free TRC105 1 h before ^{64}Cu -CuS@MSN-TRC105 ($\sim 1 \text{ mg/kg}$) injection could significantly reduce the tumor uptake to 3.0 ± 0.1 and $2.3 \pm 0.3\% \text{ ID/g}$ at 4 and 24 h p.i., respectively ($n = 3$, Figure 4c), clearly demonstrating CD105 specificity of ^{64}Cu -CuS@MSN-TRC105 *in vivo*. Figure 4d also summarizes the comparison of 4T1 tumor uptake of the three groups at different time points, with ^{64}Cu -CuS@MSN-TRC105 showing the highest tumor uptake throughout the study period. An *ex vivo* histology study further confirmed the vasculature targeting of ^{64}Cu -CuS@MSN-TRC105, as evidenced by the desirable overlay of the red (representing CD31 from tumor vasculature) and green fluorescence signals (representing TRC105 from ^{64}Cu -CuS@MSN-TRC105) in the tumor tissue slices (Figure 4e). No observable green fluorescence was detected in muscle, which is consistent with the PET imaging results (Figure 4a,e). The *in vivo* specific vasculature targeting of ^{64}Cu -CuS@MSN-TRC105 was demonstrated through these studies.

CONCLUSIONS

In conclusion, a new type of CuS@MSN based theranostic nanoparticle was designed, synthesized, and surface engineered for tumor vasculature targeting and photothermal therapy. Successful synthesis of

CuS@MSN was found to be highly dependent on the surface charge of the CuS nanoparticle and the excess of surfactant CTAC. *In vivo* therapeutic evaluations in 4T1 tumor-bearing mice showed a complete photothermal ablation of tumors after laser excitation with no tumor regrowth over two months. A long-term toxicity study with a large dose of nanoparticles showed only minor *in vivo* toxicity. After conjugation with the TRC105 antibody, we also demonstrated the specific and significantly enhanced tumor vasculature

targeting of ^{64}Cu -CuS@MSN-TRC105 *in vivo*, which was further confirmed by the *ex vivo* biodistribution and histology studies. To the best of our knowledge, as-developed ^{64}Cu -CuS@MSN-TRC105 is one of the very few theranostic nanoparticles that possess the capability for *in vivo* active tumor targeting. We are currently investigating the potential of these nanoparticles for *in vivo* tumor targeted photothermally enhanced drug delivery and thermo-chemotherapy.

MATERIALS AND METHODS

Materials. TRC105 was provided by TRACON Pharmaceuticals Inc. (San Diego, CA). *p*-SCN-Bn-NOTA (*i.e.*, 2-S-(4-isothiocyanatobenzyl)-1,4,7-triazacyclonane-1,4,7-triacetic acid) was acquired from Macrocyclics, Inc. (Dallas, TX). NHS-fluorescein, hematoxylin staining solution, and Chelex 100 resin (50–100 mesh), tetraethyl orthosilicate (TEOS), triethanolamine (TEA), (3-Aminopropyl)triethoxysilane (APS), Cetyltrimethylammonium chloride solution (CTAC, 25 wt %), copper(II) chloride (CuCl_2), sodium sulfide nonahydrate ($\text{Na}_2\text{S} \cdot 9\text{H}_2\text{O}$) and sodium citrate dehydrate were purchased from Sigma-Aldrich (St. Louis, MO). AlexaFluor488- and Cy3-labeled secondary antibodies were purchased from Jackson ImmunoResearch Laboratories, Inc. (West Grove, CA). PD-10 columns were purchased from GE Healthcare (Piscataway, NJ). Absolute ethanol, sodium chloride (NaCl), doxorubicin hydrochloride (DOX) were purchased from Fisher Scientific. SCM-PEG_{5k}-Mal was obtained from Creative PEG-works. Water and all buffers were of Millipore grade and pretreated with Chelex 100 resin to ensure that the aqueous solution was free of heavy metals. All chemicals were used as received without further purification.

Synthesis of Sodium Citrate Capped CuS Nanoparticles. Previously reported procedures were used for the synthesis of CuS-Cit with slightly modifications.¹⁰ For a typical synthesis, 10 mL of CuCl_2 water solution (0.85 mg/mL) and 10 mL of sodium citrate (1.0 mg/mL) were added into 30 mL of water. The mixture was stirred for 30 min at room temperature. After that, 50 μL of Na_2S (60.54 mg/250 μL) was added to the mixture and stirred for another 5 min before transferring to a 90 °C water bath. The reaction was kept for 15 min before cooling down with ice, forming green-colored CuS-Cit nanoparticles.

Synthesis of CTAC Capped CuS Nanoparticles. For the synthesis of CTAC-capped CuS nanoparticles, 10 mL of CuCl_2 water solution (0.85 mg/mL) and 40 μL of CTAC (25 wt % solution) were added into 40 mL of water. The mixture was stirred for 30 min at room temperature. After that, 50 μL of Na_2S (60.54 mg/250 μL) was added to the mixture and stirred for another 5 min before transferring to a 90 °C water bath. Green colored CuS-CTAC nanoparticle would form after 15 min reaction.

Synthesis of CuS@MSN and CuS@MSN-NH₂. In a typical synthesis, CTAC (2 g, 25 wt % solution) and TEA (20 mg) were dissolved in 20 mL of preprepared CuS-CTAC water solution, and stirred at room temperature for 1 h. Then, 200 μL of TEOS was added at a rate of 40 $\mu\text{L}/\text{min}$ and the resulting mixture was stirred for another 1 h at 85–90 °C water bath. The mixture was then cool down, collected by centrifugation and washed with water to remove residual reactants. Then, the products were extracted for 24 h with a 1 wt % solution of NaCl in methanol to remove the template CTAC. This process was carried out for at least 3 times to make sure all of the CTAC has been removed. For amino group modification, 20 mL (2 mg/mL) CuS@MSN in absolute ethanol was reacted with APS (1 mL) at room temperature for 48 h to form CuS@MSN-NH₂. The final sample was washed with ethanol for multiple times to get rid of free APS. The concentration of –NH₂ groups (nmol/mL) was measured using a Kaiser test kit.

Photothermal Effect of CuS@MSN in Water. To study the photothermal effect of CuS@MSN in water, CuS@MSN with varied

concentration, ranging from 0 to 0.5 mM (based on the total amount of Cu measured by using ICP-AES testing), was suspended in water, and subjected to 980 nm laser irradiation for 5 min. The temperature change in water was monitored by using a digital thermometer. 980 nm laser with different laser power density (*i.e.*, 0.5, 1.0, 2.0, 4.0 W/cm²) was also used.

Loading CuS@MSN with Hydrophilic Anticancer Drugs. Successful loading of hydrophilic drugs, *e.g.*, DOX, into meso-channels from CuS@MSN was achieved thanks to its large surface area (495 m²/g) and pore volume (0.68 cm³/g). CuS@MSN with a known mass (0.6 mg) was resuspended in 0.5 mg/mL of DOX-PBS solution (total amount of DOX was 0.3 mg). The mixture was kept under constant shaking for 24 h at room temperature. Afterward, CuS@MSN(DOX) was collected by centrifugation and washed with PBS for 3 times. All DOX in supernatant was carefully collected and quantified based on DOX (in PBS solution) standard curve. The loading capacity was calculated by the following equation: loading capacity % = Amount of DOX in CuS@MSN/Mass of CuS@MSN*100.

Thiolation of TRC105. For the thiolation of TRC105 antibody, in 500 μL (5 mg/mL) of TRC105 added 50 μL (2 mg/mL) of fresh-made Traut's Reagent, and adjusted the pH to 8.0 using 0.1 M Na₂CO₃. The mixture was kept shaking for 2 h at room temperature. As-synthesized TRC105-SH was purified using PD-10 columns with PBS as the mobile phase. Fraction from 3.0 to 4.0 mL was collected and concentrated using a 10 kDa centrifugal filter (Microcon) at 5000 rpm for 15 min. The final concentration of TRC105-SH was quantified using Nanodrop, and the number of –SH groups per TRC105 was estimated to be 5–6 based on Ellman's Reagent testing.

Synthesis of NOTA-CuS@MSN-PEG_{5k}-TRC105. To conjugate CuS@MSN-NH₂ with NOTA, *p*-SCN-Bn-NOTA (~53 nmol) in dimethyl sulfoxide (DMSO) was allowed to react with CuS@MSN-NH₂ (~2 mg/mL) at pH 8.5 for 2 h to obtain NOTA-CuS@MSN-NH₂. Afterward, 5 mg (1000 nmol) of SCM-PEG_{5k}-Mal was added into NOTA-CuS@MSN-NH₂ water solution (pH 7), and reacted for another 60 min, resulting in NOTA-CuS@MSN-PEG_{5k}-Mal. The PEGylated sample was isolated by centrifugation at 10 k rpm for 10 min. Free PEG was removed by washing with PBS for at least 2 times. NOTA-CuS@MSN-PEG_{5k}-TRC105 could be obtained by reacting TRC105-SH (2.5 nmol) with NOTA-CuS@MSN-PEG_{5k}-Mal for 2 h at room temperature. Half of the NOTA-CuS@MSN-PEG_{5k}-Mal from the same batch was saved as the nontargeted group to ensure equal amount of NOTA and PEG in the final nontargeted nanoconjugates.

Since all the CuS@MSN conjugates will contain the same NOTA and PEG chains (5 kDa), both "NOTA" and "PEG_{5k}" were omitted from the acronyms of the final conjugates for clarity considerations. The final nanoconjugates were short for CuS@MSN-TRC105.

In Vitro CD105 Targeting. Flow cytometry study was performed to study the *in vitro* CD105 targeting capability of fluorescein conjugated CuS@MSN-TRC105. Cells were first harvested and suspended in cold PBS with 2% bovine serum albumin at a concentration of 5×10^6 cells/mL, and then incubated with fluorescein conjugated CuS@MSN-TRC105 (targeted group) or fluorescein conjugated CuS@MSN (nontargeted group) for 30 min at room temperature. Then, they were washed three

times with cold PBS, and centrifuged for 5 min. Afterward, the cells were washed and analyzed using a BD FACSCalibur four-color analysis cytometer, which is equipped with 488 and 633 nm lasers (Becton-Dickinson, San Jose, CA) and FlowJo analysis software (Tree Star, Ashland, OR). “Blocking” experiment was also performed in cells incubated with same amount of fluorescein conjugated CuS@MSN-TRC105, where 500 μ g/mL of free TRC105 was added to evaluate the CD105 specificity of fluorescein conjugated CuS@MSN-TRC105.

In Vivo Long-Term Toxicity Study of PEGylated CuS@MSN. To study the potential toxicity of CuS@MSN, a large dose (90 mg/kg) of PEGylated CuS@MSN was intravenous (i.v.) injected to healthy female BALB/c mice (weight: ~18 g, $n = 3$). The fluctuation of mouse body weight was monitored every other day for over 2 months. H&E staining of tissues from heart, liver, spleen, lung and kidney was conducted after Day 60 to further investigate the potential signs of toxicity (*i.e.*, cellular shrinkage or blebbing, steatosis in liver cells, condensation of chromatin, rupture of cell membrane and apoptotic bodies).

Copper-64 (^{64}Cu) Labeling. ^{64}Cu was produced via a $^{64}\text{Ni}(\text{p},\text{n})^{64}\text{Cu}$ reaction using a cyclotron at the University of Wisconsin – Madison. For a typical radiolabeling, $^{64}\text{CuCl}_2$ (74–148 MBq) was diluted in 300 μL of 0.1 M sodium acetate buffer ($\text{pH} = 6.5$) and added to 80 μL of NOTA-CuS@MSN-PEG_{5k}-TRC105 (~80 μg) or NOTA-CuS@MSN-PEG_{5k} (~80 μg). The reaction was allowed to proceed at 37 °C for 30 min with constant stirring. ^{64}Cu -NOTA-CuS@MSN-PEG_{5k}-TRC105 and ^{64}Cu -NOTA-CuS@MSN-PEG_{5k} were purified using PD-10 columns with PBS as the mobile phase. Final nanoconjugates were short for ^{64}Cu -CuS@MSN-TRC105 (targeted group) and ^{64}Cu -CuS@MSN (nontargeted group).

4T1 Tumor Model. To generate the 4T1 tumor model, 4 to 5 week old female BALB/c mice were purchased from Harlan (Indianapolis, IN, USA), and tumors were established by subcutaneously injecting 2×10^6 cells, suspended in 100 μL of 1:1 mixture of RPMI 1640 and Matrigel (BD Biosciences, Franklin Lakes, NJ, USA), into the front flank of mice. The tumor sizes were monitored every other day, and the animals were subjected to *in vivo* experiments when the tumor diameter reached 5–8 mm.

In Vivo Photothermal Ablation. *In vivo* photothermal ablation of tumor was also demonstrated after a single intratumoral injection of ~50 μL of CuS@MSN in 4T1 tumor-bearing mice ($n = 5$, dose: 33 mg/kg). Tumors were irradiated with 980 nm laser (4 W/cm²) for 15 min (the laser irradiation was stopped for 1 min after every 5 min treatment in order to avoid the overheating), followed by size measurement with a caliper every other day. The tumor sizes were calculated as the volume = (tumor length) \times (tumor width)²/2. Two control groups, *i.e.*, (CuS@MSN only) and (980 nm laser only), were also introduced to better demonstrate the photothermal ablation property.

In Vivo Vasculature Targeted PET Imaging. All animal studies were conducted under a protocol approved by the University of Wisconsin Institutional Animal Care and Use Committee. PET scans at various time points postinjection (p.i.) using a micro-PET/microCT Inveon rodent model scanner (Siemens Medical SolutionsUSA, Inc.), image reconstruction, and region-of-interest (ROI) analysis of the PET data were performed similar as described previously.³⁴ Quantitative PET data were presented as percentage injected dose per gram of tissue (% ID/g). 4T1 murine breast tumor-bearing mice, a fast-growing tumor model with high CD105 expression on the tumor vasculature, were each i.v. injected with ~10 MBq of ^{64}Cu -CuS@MSN-TRC105 (targeted group, dose: ~1 mg/kg) or ^{64}Cu -CuS@MSN (nontargeted group, dose: ~1 mg/kg) via tail vein before serial PET scans. Another group of four 4T1 tumor-bearing mice were each injected with 1 mg of unlabeled TRC105 at 1 h before ^{64}Cu -CuS@MSN-TRC105 (dose: ~1 mg/kg) administration to evaluate the CD105 specificity of ^{64}Cu -CuS@MSN-TRC105 *in vivo* (*i.e.*, blocking group).

Ex Vivo Biodistribution Study. After the last PET scans at 24 h p.i., biodistribution studies were carried out to confirm that the % ID/g values based on PET imaging truly represented the radioactivity distribution in tumor-bearing mice. Mice were euthanized, and blood, 4T1 tumor, and major organs/tissues were collected and wet-weighed. The radioactivity in the tissue

was measured using a gamma-counter (PerkinElmer) and presented as % ID/g (mean \pm SD).

Histology. All images were acquired with a Nikon Eclipse Ti microscope. Frozen tissue slices of 7 μm were fixed with cold acetone and stained for endothelial marker CD31, as described previously through the use of a rat antimouse CD31 antibody and a Cy3-labeled donkey antirat IgG.^{35,36} The tissue slices were also incubated with 2 $\mu\text{g}/\text{mL}$ of AlexaFluor488-labeled goat antihuman IgG for visualization of CuS@MSN-TRC105 (no unconjugated TRC105 was used for histology).

Conflict of Interest: The authors declare the following competing financial interest(s): Charles P. Theuer is an employee of TRACON.

Acknowledgment. This work is supported, in part, by the University of Wisconsin – Madison, the National Institutes of Health (NIBIB/NCI 1R01CA169365 and T32CA009206, P30CA014520), the Department of Defense (W81XWH-11-0-044), and the American Cancer Society (125246-RSG-13-099-01-CCE).

Supporting Information Available: Figures S1–S13. This material is available free of charge via the Internet at <http://pubs.acs.org>.

REFERENCES AND NOTES

- Jokerst, J. V.; Gambhir, S. S. Molecular Imaging with Theranostic Nanoparticles. *Acc. Chem. Res.* **2011**, *44*, 1050–1060.
- Blackwell, K. L.; Burstein, H. J.; Storniolo, A. M.; Rugo, H. S.; Sledge, G.; Aktan, G.; Ellis, C.; Florance, A.; Vukelja, S.; Bischoff, J.; et al. Overall Survival Benefit with Lapatinib in Combination with Trastuzumab for Patients with Human Epidermal Growth Factor Receptor 2-Positive Metastatic Breast Cancer: Final Results from the EGF104900 Study. *J. Clin. Oncol.* **2012**, *30*, 2585–2592.
- Benezra, M.; Penate-Medina, O.; Zanzonico, P. B.; Schaer, D.; Ow, H.; Burns, A.; DeStanchina, E.; Longo, V.; Herz, E.; Iyer, S.; et al. Multimodal Silica Nanoparticles Are Effective Cancer-Targeted Probes in a Model of Human Melanoma. *J. Clin. Invest.* **2011**, *121*, 2768–2780.
- Chen, F.; Cai, W. Tumor Vasculature Targeting: A Generally Applicable Approach for Functionalized Nanomaterials. *Small* **2014**, *10*, 1887–1893.
- Xie, J.; Lee, S.; Chen, X. Nanoparticle-Based Theranostic Agents. *Adv. Drug Delivery Rev.* **2010**, *62*, 1064–1079.
- Lammers, T.; Aime, S.; Hennink, W. E.; Storm, G.; Kiessling, F. Theranostic Nanomedicine. *Acc. Chem. Res.* **2011**, *44*, 1029–1038.
- Ahmed, N.; Fessi, H.; Elaissari, A. Theranostic Applications of Nanoparticles in Cancer. *Drug Discovery Today* **2012**, *17*, 928–934.
- Muthu, M. S.; Leong, D. T.; Mei, L.; Feng, S.-S. Nanotheranostics—Application and Further Development of Nanomedicine Strategies for Advanced Theranostics. *Theranostics* **2014**, *4*, 660–677.
- Chen, F.; Ehlerding, E. B.; Cai, W. Theranostic Nanoparticles. *J. Nucl. Med.* **2014**, *55*, 1919–1922.
- Zhou, M.; Zhang, R.; Huang, M.; Lu, W.; Song, S.; Melancon, M. P.; Tian, M.; Liang, D.; Li, C. A Chelator-Free Multifunctional [64Cu]CuS Nanoparticle Platform for Simultaneous Micro-Pet/Ct Imaging and Photothermal Ablation Therapy. *J. Am. Chem. Soc.* **2010**, *132*, 15351–15358.
- Rosen, L. S.; Hurwitz, H. I.; Wong, M. K.; Goldman, J.; Mendelson, D. S.; Figg, W. D.; Spencer, S.; Adams, B. J.; Alvarez, D.; Seon, B. K.; et al. A Phase I First-in-Human Study of TRC105 (Anti-Endoglin Antibody) in Patients with Advanced Cancer. *Clin. Cancer Res.* **2012**, *18*, 4820–4829.
- Tian, Q.; Jiang, F.; Zou, R.; Liu, Q.; Chen, Z.; Zhu, M.; Yang, S.; Wang, J.; Wang, J.; Hu, J. Hydrophilic Cu₉S₅ Nanocrystals: A Photothermal Agent with a 25.7% Heat Conversion Efficiency for Photothermal Ablation of Cancer Cells *In Vivo*. *ACS Nano* **2011**, *5*, 9761–9771.
- Tian, Q.; Tang, M.; Sun, Y.; Zou, R.; Chen, Z.; Zhu, M.; Yang, S.; Wang, J.; Wang, J.; Hu, J. Hydrophilic Flower-Like Cu

- Superstructures as an Efficient 980 nm Laser-Driven Photothermal Agent for Ablation of Cancer Cells. *Adv. Mater.* **2011**, *23*, 3542–3547.
14. U.S. Food and Drug Administration. Select Committee on GRAS Substances (SCOGS) Opinion: Silicon Dioxides, <http://www.fda.gov/food/ingredientspackaginglabeling/gras/scogs/ucm261095.htm>.
 15. Shen, D.; Yang, J.; Li, X.; Zhou, L.; Zhang, R.; Li, W.; Chen, L.; Wang, R.; Zhang, F.; Zhao, D. Biphase Stratification Approach to Three-Dimensional Dendritic Biodegradable Mesoporous Silica Nanospheres. *Nano Lett.* **2014**, *14*, 923–932.
 16. Vallet-Regi, M.; Rámila, A.; del Real, R. P.; Pérez-Pariente, J. A New Property of Mcm-41: Drug Delivery System. *Chem. Mater.* **2000**, *13*, 308–311.
 17. Pan, L.; He, Q.; Liu, J.; Chen, Y.; Ma, M.; Zhang, L.; Shi, J. Nuclear-Targeted Drug Delivery of Tat Peptide-Conjugated Monodisperse Mesoporous Silica Nanoparticles. *J. Am. Chem. Soc.* **2012**, *134*, 5722–5725.
 18. Song, G.; Wang, Q.; Wang, Y.; Lv, G.; Li, C.; Zou, R.; Chen, Z.; Qin, Z.; Huo, K.; Hu, R.; et al. A Low-Toxic Multifunctional Nanoplatform Based on Cu₉S₅@mSiO₂ Core-Shell Nanocomposites: Combining Photothermal- and Chemotherapies with Infrared Thermal Imaging for Cancer Treatment. *Adv. Funct. Mater.* **2013**, *23*, 4281–4292.
 19. Yuan, L.; Tang, Q.; Yang, D.; Zhang, J. Z.; Zhang, F.; Hu, J. Preparation of pH-Responsive Mesoporous Silica Nanoparticles and Their Application in Controlled Drug Delivery. *J. Phys. Chem. C* **2011**, *115*, 9926–9932.
 20. Manchun, S.; Dass, C. R.; Sriamornsak, P. Targeted Therapy for Cancer Using pH-Responsive Nanocarrier Systems. *Life Sci.* **2012**, *90*, 381–387.
 21. Zhan, Q.; Qian, J.; Liang, H.; Somesfalean, G.; Wang, D.; He, S.; Zhang, Z.; Andersson-Engels, S. Using 915 nm Laser Excited Tm(3+)+Er(3+)+Ho(3+)-Doped NaYF₄ Upconversion Nanoparticles for *In Vitro* and Deeper *In Vivo* Bioimaging without Overheating Irradiation. *ACS Nano* **2011**, *5*, 3744–3757.
 22. Fonsatti, E.; Sigalotti, L.; Arslan, P.; Altomonte, M.; Maio, M. Emerging Role of Endoglin (CD105) as a Marker of Angiogenesis with Clinical Potential in Human Malignancies. *Curr. Cancer Drug Targets* **2003**, *3*, 427–432.
 23. Fonsatti, E.; Nicolay, H. J.; Altomonte, M.; Covre, A.; Maio, M. Targeting Cancer Vasculature via Endoglin/CD105: A Novel Antibody-Based Diagnostic and Therapeutic Strategy in Solid Tumours. *Cardiovasc. Res.* **2010**, *86*, 12–19.
 24. Zhang, Y.; Hong, H.; Nayak, T. R.; Valdovinos, H. F.; Myklejord, D. V.; Theuer, C. P.; Barnhart, T. E.; Cai, W. Imaging Tumor Angiogenesis in Breast Cancer Experimental Lung Metastasis with Positron Emission Tomography, Near-Infrared Fluorescence, and Bioluminescence. *Angiogenesis* **2013**, *16*, 663–674.
 25. Orbay, H.; Zhang, Y.; Hong, H.; Hacker, T. A.; Valdovinos, H. F.; Zagzebski, J. A.; Theuer, C. P.; Barnhart, T. E.; Cai, W. Positron Emission Tomography Imaging of Angiogenesis in a Murine Hindlimb Ischemia Model with ⁶⁴Cu-Labeled TRC105. *Mol. Pharmaceutics* **2013**, *10*, 2749–2756.
 26. Orbay, H.; Zhang, Y.; Valdovinos, H. F.; Song, G.; Hernandez, R.; Theuer, C. P.; Hacker, T. A.; Nickles, R. J.; Cai, W. Positron Emission Tomography Imaging of CD105 Expression in a Rat Myocardial Infarction Model with ⁶⁴Cu-NOTA-TRC105. *Am. J. Nucl. Med. Mol. Imaging* **2013**, *4*, 1–9.
 27. Hong, H.; Yang, K.; Zhang, Y.; Engle, J. W.; Feng, L.; Yang, Y.; Nayak, T. R.; Goel, S.; Bean, J.; Theuer, C. P.; et al. *In Vivo* Targeting and Imaging of Tumor Vasculature with Radiolabeled, Antibody-Conjugated Nanographene. *ACS Nano* **2012**, *6*, 2361–2370.
 28. Chen, F.; Hong, H.; Shi, S.; Goel, S.; Valdovinos, H. F.; Hernandez, R.; Theuer, C. P.; Barnhart, T. E.; Cai, W. Engineering of Hollow Mesoporous Silica Nanoparticles for Remarkably Enhanced Tumor Active Targeting Efficacy. *Sci. Rep.* **2014**, *4*, 5080.
 29. Chen, F.; Hong, H.; Zhang, Y.; Valdovinos, H. F.; Shi, S.; Kwon, G. S.; Theuer, C. P.; Barnhart, T. E.; Cai, W. *In Vivo* Tumor Targeting and Image-Guided Drug Delivery with Antibody-Conjugated, Radiolabeled Mesoporous Silica Nanoparticles. *ACS Nano* **2013**, *7*, 9027–9039.
 30. Guo, J.; Hong, H.; Chen, G.; Shi, S.; Zheng, Q.; Zhang, Y.; Theuer, C. P.; Barnhart, T. E.; Cai, W.; Gong, S. Image-Guided and Tumor-Targeted Drug Delivery with Radiolabeled Unimolecular Micelles. *Biomaterials* **2013**, *34*, 8323–8332.
 31. Wu, W.; Ichihara, G.; Hashimoto, N.; Hasegawa, Y.; Hayashi, Y.; Tada-Oikawa, S.; Suzuki, Y.; Chang, J.; Kato, M.; D'Alessandro-Gabazza, C. N.; et al. Synergistic Effect of Bolus Exposure to Zinc Oxide Nanoparticles on Bleomycin-Induced Secretion of Pro-Fibrotic Cytokines without Lasting Fibrotic Changes in Murine Lungs. *Int. J. Mol. Sci.* **2015**, *16*, 660–676.
 32. Hong, H.; Zhang, Y.; Sun, J.; Cai, W. Molecular Imaging and Therapy of Cancer with Radiolabeled Nanoparticles. *Nano Today* **2009**, *4*, 399–413.
 33. Seon, B. K.; Haba, A.; Matsuno, F.; Takahashi, N.; Tsujie, M.; She, X.; Harada, N.; Ueda, S.; Tsujie, T.; Toi, H.; et al. Endoglin-Targeted Cancer Therapy. *Curr. Drug Delivery* **2011**, *8*, 135–143.
 34. Hong, H.; Zhang, Y.; Severin, G. W.; Yang, Y.; Engle, J. W.; Niu, G.; Nickles, R. J.; Chen, X.; Leigh, B. R.; Barnhart, T. E.; et al. Multimodality Imaging of Breast Cancer Experimental Lung Metastasis with Bioluminescence and a Monoclonal Antibody Dual-Labeled with ⁸⁹Zr and IRdye 800CW. *Mol. Pharmaceutics* **2012**, *9*, 2339–2349.
 35. Cai, W.; Zhang, X.; Wu, Y.; Chen, X. A Thiol-Reactive 18f-Labeling Agent, N-[2-(4-18f-Fluorobenzamido)Ethyl]-Maleimide, and Synthesis of RGD Peptide-Based Tracer for PET Imaging of Alpha V Beta 3 Integrin Expression. *J. Nucl. Med.* **2006**, *47*, 1172–1180.
 36. Cai, W.; Wu, Y.; Chen, K.; Cao, Q.; Tice, D. A.; Chen, X. *In Vitro* and *In Vivo* Characterization of ⁶⁴Cu-Labeled Abegrin, a Humanized Monoclonal Antibody against Integrin Alpha V Beta 3. *Cancer Res.* **2006**, *66*, 9673–9681.